

See discussions, stats, and author profiles for this publication at: <https://www.researchgate.net/publication/27257607>

Subsurface Oxygen in the CO Oxidation Reaction on Pt(110): Experiments and Modeling of Pattern Formation

ARTICLE *in* THE JOURNAL OF PHYSICAL CHEMISTRY B · JUNE 1998

Impact Factor: 3.3 · DOI: 10.1021/jp981285t · Source: OAI

CITATIONS

57

READS

15

4 AUTHORS, INCLUDING:



[Alexander S. Mikhailov](#)

Fritz Haber Institute of the Max Planck Society

285 PUBLICATIONS 6,220 CITATIONS

SEE PROFILE



[Harm Hinrich Rotermund](#)

Dalhousie University

140 PUBLICATIONS 5,071 CITATIONS

SEE PROFILE

Subsurface Oxygen in the CO Oxidation Reaction on Pt(110): Experiments and Modeling of Pattern Formation

Alexander von Oertzen,* Alexander S. Mikhailov, Harm H. Rotermund, and Gerhard Ertl

Fritz-Haber-Institut der Max-Planck-Gesellschaft, Faradayweg 4-6, D-14195 Berlin, Germany

Received: February 25, 1998; In Final Form: March 31, 1998

New experimental evidence on the formation of spatio-temporal concentration patterns as imaged by photoemission electron microscopy (PEEM) supports our earlier kinetic model for subsurface oxygen formation in the CO oxidation reaction on Pt(110). Extensive experimental data on oxygen island growth and conversion is used to derive the activation energy and the preexponential factor for the process of subsurface oxygen formation. We find that under reaction conditions formation of subsurface oxygen may significantly influence properties of traveling concentration waves. Instead of annihilation of two colliding waves, their reflection and two-into-one collision events are observed in the experiments. This behavior is correctly reproduced by the model.

1. Introduction

Chemical reactions, which show complex phenomena of pattern formation, have recently moved into the focus of the research interest. Among others, catalytic reactions on single crystal surfaces play a particular role not only because of their practical importance, but also due to the relative simplicity of their mechanisms. Moreover, their intrinsically two-dimensional geometry allows to apply various observation methods, ranging from optical and electron microscopy to scanning tunneling microscopy, and thus to directly study the reaction process down to the atomic resolution.

The CO oxidation reaction on Pt(110) is one of the most thoroughly investigated systems of this type.^{1–3} Molecular beam investigations⁴ have shown that this reaction proceeds via the Langmuir–Hinshelwood mechanism (i.e., CO and oxygen have to adsorb before the reaction to CO₂ can take place). Results for the adsorption kinetics of oxygen^{5–7} and of CO^{8–11} were reported at about the same time when the first kinetic self-sustained oscillations on a single crystal were observed.¹² Understanding of the phase transition role^{13–15} has finally led to the formulation of the first detailed model of this catalytic reaction.^{16,17}

To explain properties of spatio-temporal pattern formation, this model has been extended to include diffusion of CO molecules on the surface.^{18,19} The simulations have shown that the model contains solutions, corresponding to traveling waves of chemical concentrations, and that these solutions agree with the experimental observations.¹⁸ It has also been found that most of this behavior can already be described²⁰ by a reduced version of the model containing only two variables and representing a variant of the well-known FitzHugh–Nagumo model. This model has been successfully applied, for example, to understand properties of spiral waves under conditions of external forcing²¹ and for local modifications of the catalyst surface.^{22,23}

Further analysis of the experimental data for the CO oxidation reaction on Pt and for other reactions, such as NO+H₂ on Rh^{24,25}

or NO+CO on Pt,^{26,27} has shown that additional aspects should be incorporated into the models of these reactions. General effects of complex diffusion anisotropy have been considered^{28,29} and various models, including global coupling through the gas phase, have been investigated.^{30–36}

Most of the above models aimed only at qualitative or semiquantitative agreement with the experimental data. It was, however, believed that they already included all basic mechanistic details of the reaction and good quantitative agreement could, in principle, be achieved by careful fitting of the model parameters (and, perhaps, incorporation of various phenomenological coverage dependences of the reaction rate constants^{37–39}).

Quite surprisingly the experiments on oxygen island conversion^{40,41} have clearly shown that yet another species, namely *subsurface oxygen*, was also involved in the reaction of CO oxidation on Pt(110) (this has also been earlier suggested as a possible interpretation of some thermal desorption spectroscopy experiments⁴²). By analyzing the experimental data, we have proposed a generalization of the previous model that additionally included formation and release of subsurface oxygen and described its influence on the phase transition in the topmost substrate layer.⁴⁰ As we show in the present work, formation of subsurface oxygen takes place also under the reaction conditions and can in some cases significantly influence the properties of wave patterns observed in the reaction.

The paper consists of two parts. First we report new detailed experimental investigations of the oxygen island conversion phenomena. Furthermore, we present the results of PEEM observations under reaction conditions that show a new class of patterns (i.e., traveling bright wave fragments). These waves have unusual properties. Instead of annihilation, typical for previously observed oxygen waves in the same reaction, their frontal collisions result in reflections or fusion of two fragments and formation of a single traveling fragment.

In the second theoretical part we use the new experimental data on island conversion to determine more accurately the model parameters, specifying the processes related to subsurface oxygen. We show that, by fitting the activation energies and the preexponential factors of these processes, satisfactory quantitative agreement with the experiments in a wide temper-

* Corresponding author. E-mail: oertzen@fhi-berlin.mpg.de. FAX: + 49 – 30 – 84 13 51 06.

ature interval can be achieved. Subsequently, we use the same model to investigate properties of traveling wave patterns under the reaction conditions. Our numerical simulation show that the model reproduces the new class of patterns (i.e., the bright traveling fragments) and adequately describes their interactions.

2. Experiments

2.1. Experimental Methods. The Pt(110) single-crystal surface is kept in a ultrahigh vacuum (UHV) apparatus equipped with LEED/Auger, a quadrupole mass spectrometer, an Ar-ion sputtering gun, and a resistive sample heating used to prepare and characterize the surface. A photoemission electron microscope (PEEM)⁴³ provides information on the lateral distribution of reacting species on the surface. Gas supplies for CO and O₂ as well as pressure gauges allow for controlled dosing of the reactants into the UHV chamber. With the combination of feedback-regulated gas dosing and of permanent pumping of the chamber the CO oxidation reaction can be observed under constant flow conditions. Further details concerning the experimental and gas dosing setup can be found in earlier publications.⁴⁴

The PEEM produces images of the patterns of photoelectrons emitted by a surface under ultraviolet light irradiation. With a maximum field of view of up to 500 μm diameter, the spatial resolution of images is typically 1 μm . The PEEM is therefore not directly sensitive to molecular adsorbate coverages, but images only the change of the work function of the clean surface due to the presence of an adsorbate. For the involved species (i.e., CO, oxygen, and subsurface oxygen, these work function changes are only known for CO and oxygen). A full coverage by CO molecules increases the work function of Pt(110) by 0.15 eV, thus reducing the photoemission signal. Oxygen increases the work function by a larger value of 0.8 eV, yielding the lowest photoemission signal or, in other words, the darkest appearance in the PEEM images. For subsurface oxygen the quantitative work function change has not yet been determined, but the increase of the PEEM intensity (=bright features) signals a pronounced decrease.

PEEM images can be viewed on the phosphorus screen of the image intensifier unit by the bare eye. For later analysis, the whole temporal evolution of this image is recorded by a camera on S-VHS videotapes, thus limiting the temporal resolution to 40 ms. For the observed phenomena this temporal resolution was always sufficient. Standard image processing on single video frames was performed with a computer including background subtraction and contrast/brightness adjustments. Image averaging of two or four video frames could be applied to improve the signal-to-noise ratio in the images.

2.2. Subsurface Oxygen Islands. Islands of adsorbed oxygen atoms on an otherwise clean surface can convert into subsurface oxygen. In the temperature range of 400–500 K, complete transition from an oxygen island to a subsurface oxygen island takes up to several minutes. To induce conversion of oxygen inside the island, a special preparation procedure has to be applied. To understand the processes, occurring during the preparatory stage, the properties of the phase transition in the upper substrate layer should be taken into account.

The Pt(110) surface shows two different surface structures.^{13–15} The clean Pt(110) surface reconstructs to a 1×2 missing row structure. However, adsorption of CO molecules beyond a critical coverage leads to a transition to the nonreconstructed 1×1 surface structure corresponding to the ideal cut through the bulk. The transition rate depends on surface temperature: at room temperature the phase transition takes about 1000 s, which is reduced to only about 2 s at $T = 500$ K.

The preparation of an adsorbate oxygen island is performed by first completely covering the surface with CO at about 400 K. Within less than a minute the surface transforms into the 1×1 phase. CO gas dosing is continued, while the crystal is cooled to a temperature around 340 K. At this temperature desorption is so slow that the CO supply can be turned off and the surface remains completely CO covered. Then O₂ is let into the UHV chamber at a pressure of 1×10^{-4} mbar. The inhibition of oxygen adsorption by the complete layer of CO adsorbate becomes evident from the PEEM images, since for the first minutes nothing seems to happen. But then small oxygen islands originate at sparsely distributed locations, seen in the PEEM image as small dark spots. They grow to elliptical islands with a speed of about 30 $\mu\text{m}/\text{min}$ in the $(1\bar{1}0)$ -direction and of about 5 $\mu\text{m}/\text{min}$ in the (001) -direction. In the experiments reproduced in Figure 1 this growth stage took 7 min yielding an island with about 200 μm length of the longer elliptical axis.

The island growth is stopped by turning off the oxygen supply. Immediate heating of the sample up to the desired temperature results in subsurface oxygen formation, as reflected by the appearance of bright features in Figure 1. If the sample, on the other hand, is left for several minutes at the preparation temperature of 342 K and then heating is started, no subsurface oxygen formation is observed, but only oxygen diffusion as reported earlier.⁴⁵ This suggests that the phase transition driven by adsorbed CO may play a decisive role here and can provide a sort of memory to the oxygen island.

The electronic control of the sample heating facility allows a maximum heating rate of 5 K/s. In the case of Figure 1, the heating procedure took, depending on the final temperature, between about 10 and 30 s.

The image series of Figure 1a–c shows the conversion of oxygen adsorbate islands to subsurface oxygen islands at three different temperatures. As outlined above, the strong increase in the PEEM image intensity is due to the work function lowering by subsurface oxygen. At any stage of the island conversion, the PEEM intensity is determined by both the adsorbed and subsurface oxygen species. The effects of these two species can at a certain moment almost completely compensate each other. For example, in the frame 3 of Figure 1c, the island has become temporarily invisible due to such a compensation resulting in an effective intensity value identical to that of the clean surface surrounding the island.

The island conversion at $T = 503$ K, shown in Figure 1c, proceeds almost uniformly. At lower temperatures, however, this process is strongly nonuniform. As seen in Figure 1a,b, it begins in the periphery of an island and a bright ring due to subsurface oxygen is formed. Later this ring spreads toward the center until full conversion is accomplished.

Conversion is accompanied by slow shrinking of the island. This shrinking is a consequence of the reaction between adsorbed oxygen within the island and the remaining CO molecules on the surface. During the preparation, the island is surrounded by CO. When the temperature is increased and CO desorption is initiated, not all CO molecules will immediately desorb from the surface but some will react with adsorbed oxygen.

In Figure 1c the converted bright island (frame 6) is smaller than the initial adsorbate oxygen island of frame 1. Moreover, brightness of the region surrounding the island is decreasing from frame 1 to frame 2. Both observations are attributed to reaction with CO that is initially still present on the surface (frame 1). In frame 2 it has practically desorbed and also

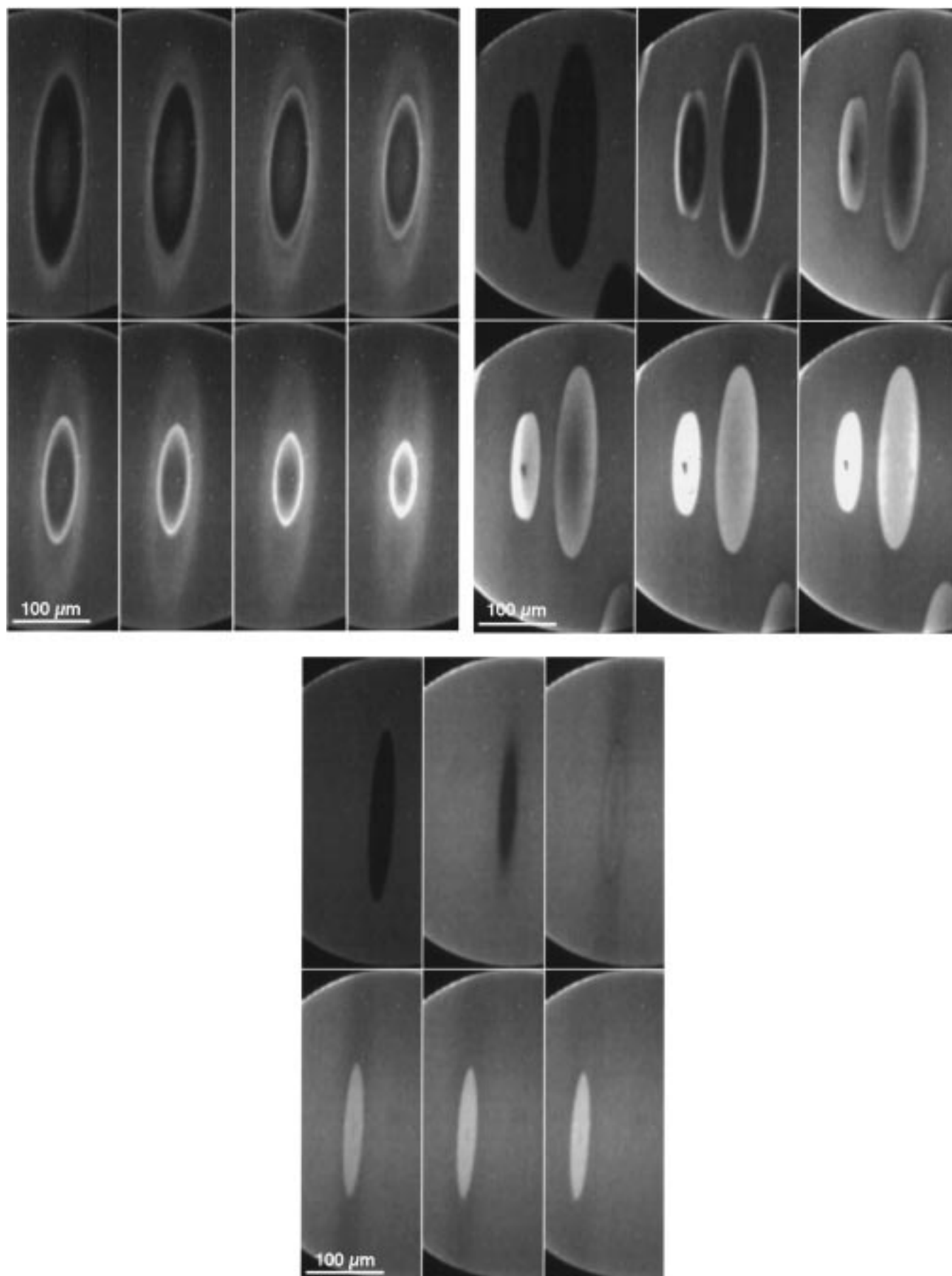


Figure 1. Conversion of oxygen islands. Subsequent PEEM images separated by equal time intervals Δt are shown from top left to bottom right. The parameters are: (a) $T = 400$ K, $\Delta t = 120$ s, image size $150 \mu\text{m} \times 420 \mu\text{m}$; (b) $T = 453$ K, $\Delta t = 60$ s, $220 \mu\text{m} \times 420 \mu\text{m}$; and (c) $T = 503$ K, $\Delta t = 30$ s, $165 \mu\text{m} \times 420 \mu\text{m}$.

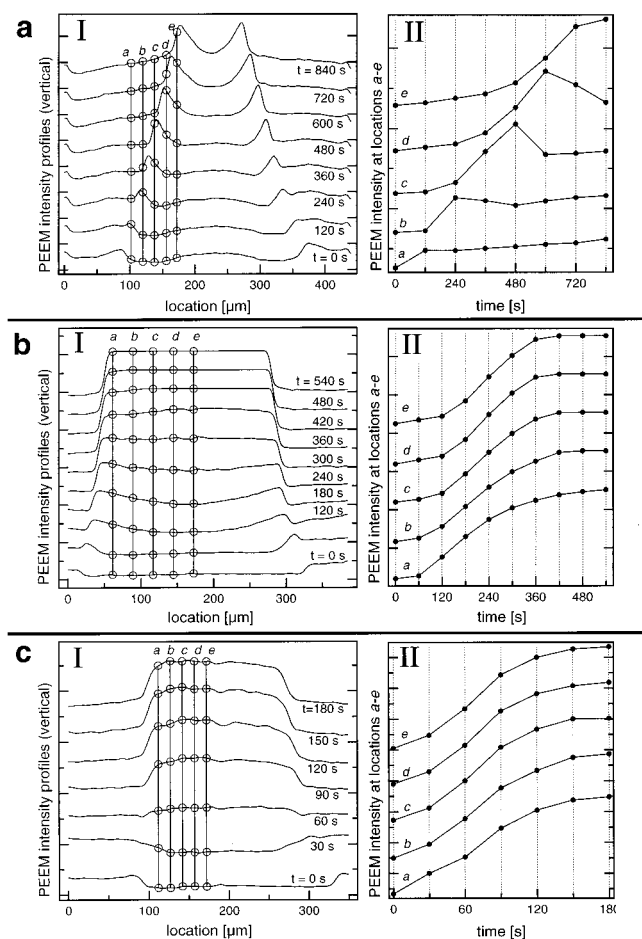


Figure 2. Spatial and temporal profiles of PEEM intensity at temperatures (a) $T = 400$ K, (b) $T = 453$ K, and (c) $T = 503$ K. The spatial profiles (I) are taken along the vertical central cross-sections in the images shown in Figure 1a–c. The profiles corresponding to subsequent frames are shifted upward to eliminate their overlaps. The temporal profiles (II) are obtained by following evolution of the PEEM intensity at several selected points *a*, *b*, *c*, *d*, and *e* that are indicated in the plots (I).

effected the island shrinking by reacting with the oxygen. At 453 K (Figure 1b) a similar effect can be observed through frames 1 and 2. Here the independent conversion of two islands of different sizes can be observed, the smaller one reaching its final bright stage earlier than the larger island.

Bright islands are quite stable for up to 30 min. Only at 400 K [Figure 1a] where the temperature is too low to cause rapid CO desorption, relatively fast gradual shrinking of the island is observed. In the area left behind the retreating island, a different gray level is seen, brighter than that of the partially CO-covered area around the island but darker than in the regions where subsurface oxygen is present. It corresponds to the almost clean surface, left after the CO+O reaction has taken place there.

Figure 2 shows the development of the PEEM intensity profiles with time at a few selected locations. The characteristic conversion time can be estimated from these plots. Additionally, the time delay of conversion between the periphery and the center of the island, that characterizes the degree of inhomogeneity of the island conversion, can be deduced from these data. In Figure 2c, the conversion curves at different locations are almost parallel. In contrast to this, a temporal shift of 60–100 s is seen in Figure 2b. Strong shrinking is the dominant process in the curves shown in Figure 2a. These plots will be analyzed in detail in the second part of this paper, where such time development is reproduced in numerical simulations.

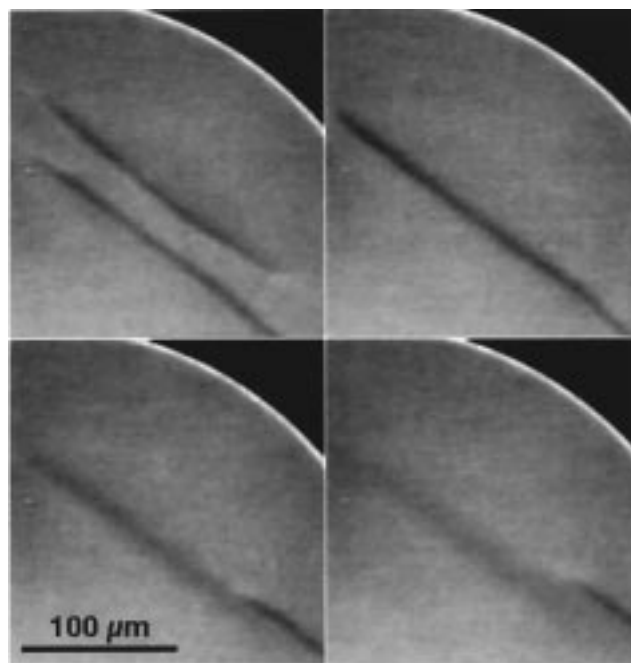


Figure 3. Collision of two oxygen waves at $T = 523$ K, $p_{\text{CO}} = 9.8 \times 10^{-5}$ mbar, and $p_{\text{O}_2} = 4 \times 10^{-4}$ mbar. The frame size is $210 \mu\text{m} \times 220 \mu\text{m}$. Four subsequent frames, separated by intervals $\Delta t = 1$ s, are shown from top left to bottom right.

Further experiments have been performed with converted oxygen islands. We have found that dosing oxygen on a converted bright island leads to darkening of the whole image, both on the free area as well as on the island. This suggests that oxygen adsorption does not seem to be significantly prevented on a subsurface oxygen covered surface. Again using a fully converted subsurface oxygen island we observe different behavior when dosing with CO. At first, we see a sudden brightness increase of the subsurface oxygen island. Then, with continued CO dosing, the island disappears within several tens of seconds. Here the speed of disappearance depends mainly on the applied CO partial pressure.

2.3. Oxygen and Subsurface Oxygen Waves. Waves of oxygen propagating on a mainly CO covered surface can be observed by PEEM, using the UHV chamber as a constant flow reactor. Both CO and O₂ are supplied through the valves at a controlled ratio. All gases, including the product CO₂, are pumped at a constant rate from the chamber. Oxygen waves are observed in the temperature range of 450–550 K. As the CO partial pressure is gradually increased, CO islands suddenly spread. Small regions of oxygen between two CO islands become dynamically unstable and start traveling in various directions. The surface oxygen waves are also generated by some defects surrounded by the CO-covered surface. These waves form spirals or, under slightly different partial pressures, traveling wave fragments.

Figure 3 shows a collision of two oxygen waves. Oxygen waves have been investigated formerly,⁴⁶ and their behavior is well described in the framework of two-component excitable and bistable media.^{18,19} The annihilation behavior as shown by Figure 3 is typical for the oxygen waves.

Subsurface oxygen waves appear in a parameter range close to the parameter range where the normal oxygen waves are seen. In contrast to normal oxygen (O_{ad}) waves, they look bright in the PEEM images. A previous treatment of the surface with oxygen island conversion experiments apparently facilitates the formation of subsurface oxygen waves instead of the oxygen

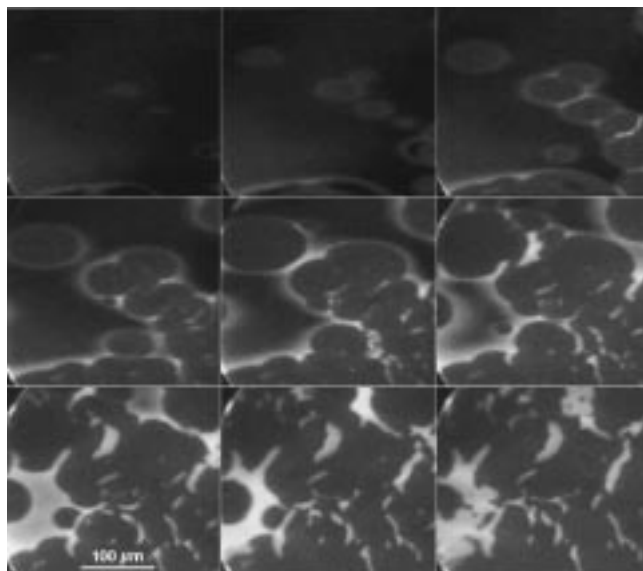


Figure 4. Formation of subsurface oxygen wave fragments (from top left to bottom right). Subsequent PEEM images of size $300\ \mu\text{m} \times 265\ \mu\text{m}$ are separated by intervals $\Delta t = 2\ \text{s}$. The reaction parameters are $T = 533\ \text{K}$, $p_{\text{CO}} = 1.8 \times 10^{-4}\ \text{mbar}$, and $p_{\text{O}_2} = 4 \times 10^{-4}\ \text{mbar}$.

waves. The properties of subsurface oxygen waves are significantly different from those of the oxygen waves.

Figure 4 shows a sequence of PEEM images illustrating how subsurface oxygen waves typically emerge in the experiments. Before the first frame in this figure the surface was completely dominated by oxygen. When the CO partial pressure is increased by 2%, CO islands originate on surface defects, as seen in the first frame. The propagating CO fronts develop bright fringes on the edges moving into the oxygen-covered surface (frame 4). These fringes look similar to those seen in the oxygen island conversion experiments (cf. Figure 1). The fringes grow, become more diffuse and spread into the oxygen-covered regions increasing their brightness (frame 6). The brightness of these image elements is much greater than that of the clean surface and we conclude that subsurface oxygen is present here.

As time goes on, the CO fronts move further into the bright regions and their area decreases. However, the shrinking bright regions do not completely disappear. Instead, we see that their further shrinking is stopped and they suddenly start to move across the surface, forming irregular bright traveling fragments as seen in the last frame in Figure 4. These bright fragments move preferentially in the crystallographic $(1\bar{1}0)$ -direction of the surface. They represent traveling waves of subsurface oxygen.

2.4. Two-into-One Collisions. In the previous section we have described how subsurface oxygen waves are typically generated. Produced in this way, the traveling subsurface oxygen fragments have largely different lengths and widths. Though they can also propagate in the orthogonal (001) surface direction, they become then very thin and easily break. Therefore, waves traveling in both directions along the (110) -axis are selected. While moving approximately in these directions, the waves undergo collisions. The collision behavior is complicated because the fragments can have different shapes and sizes, and may only partially touch each other in a collision.

In Figure 5 we have selected a frontal collision with an almost complete overlap of colliding wave fragments. The two fragments have different thickness (i.e., the right object is a little thicker than the left object). When the two waves meet



Figure 5. A typical two-into-one wave collision at $T = 533\ \text{K}$, $p_{\text{CO}} = 1.84 \times 10^{-4}\ \text{mbar}$, and $p_{\text{O}_2} = 4 \times 10^{-4}\ \text{mbar}$. Subsequent PEEM images of size $170\ \mu\text{m} \times 130\ \mu\text{m}$ are separated by equal time intervals $\Delta t = 1.92\ \text{s}$.

(frame 3), the local intensity in the collision region is significantly raised for a short period of time. The collision does not lead to annihilation of the waves. Instead, the intensity of the single fragment formed during the collision decreases to the normal intensity of subsurface oxygen waves and the fragment continues its motion in the left direction. Thus, the process shown in Figure 5 represents an example of a two-into-one collision, where two colliding fragments form a single fragment that continues its motion.

This kind of collisions between subsurface oxygen wave fragments is typically observed in the experiments whenever two colliding waves have different thickness. We always find that the thicker wave fragment takes over the thinner fragment and continues its motion. A small strongly curved fragment in the lower part of Figure 5, which has additionally emerged after the collision and travels in the right direction, may be due to a surface defect located in this area.

Figure 6a shows the intensity profiles taken at subsequent time moments along the straight line shown in frame 1 of Figure 5. The profiles corresponding to later moments are shifted in the vertical direction; they are separated by equal time intervals. The PEEM intensity increase during the collision is clearly seen in the fifth profile from the bottom. Following the positions of the pulse maxima (Figure 6b), a delay of 1.1 s in the movement of the thicker right pulse, as it goes through the collision, is detected.

2.5. Two-into-Two Collisions. Subsurface oxygen waves with other properties can also be observed during the reaction. They are found under the conditions close to those at which normal oxygen waves, forming large spirals or soliton-like waves, have previously been seen.^{46–48} The bright subsurface oxygen waves appear on the surface, if several conversion cycles of oxygen islands to subsurface oxygen have earlier been performed. Their propagation seems then to be restricted to surface areas where such conversion has previously taken place.

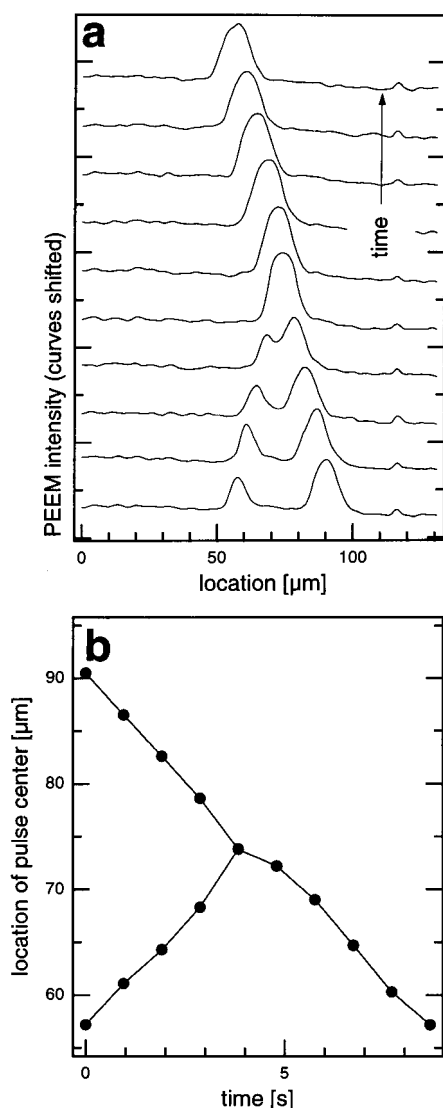


Figure 6. Spatial PEEM intensity profiles (a) and the respective time diagram (b) taken along the dashed line in Figure 5. Subsequent profiles, separated by equal intervals $\Delta t = 0.96$ s, are shifted upward to prevent their overlap. The time diagram (b) shows motion of the points corresponding to maximal PEEM intensity in the colliding pulses.

Apparently, the surface has undergone here a modification through repeated subsurface oxygen conversion experiments.

In contrast to wave fragments, described in section 2.4, no significant variation in the widths of these waves is found (i.e., all of them have the same thickness at fixed reaction parameters). As time goes on, their broken ends curl, forming traveling curved fragments [see Figure 7] and spirals. However, the growth is very slow and the shape of wave fragments often persists unchanged over large traveling distances. Collisions between such waves usually lead to annihilation. Because of repeated annihilations, the number of wave fragments is generally lower in this case than for the waves described in the previous section.

A special property of such bright wave fragments is, that under frontal collisions between them, reflections have been observed. Figure 7 shows a collision of two waves propagating along the $(1\bar{1}0)$ -axis. When the waves merge (frame 3), they form an object with an increased intensity. However, this object does not die out later. Instead, two new waves, propagating from the collision region, are generated (frames 6–8). Hence, the entire event can be characterized as a two-into-two collision.

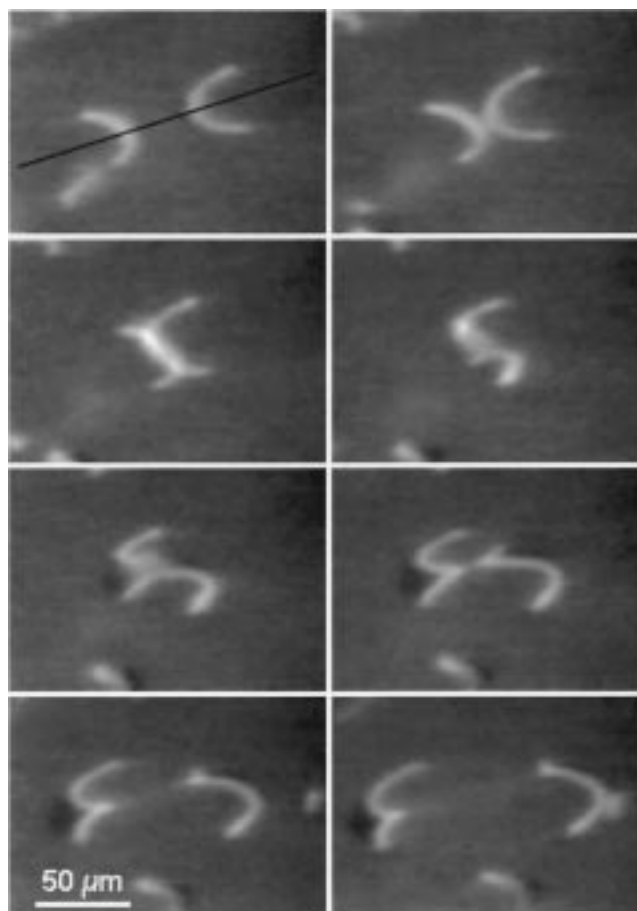


Figure 7. A wave collision of the two-into-two type. The reaction parameters are $T = 503$ K, $p_{\text{CO}} = 9 \times 10^{-5}$ mbar, and $p_{\text{O}_2} = 4 \times 10^{-4}$ mbar. Subsequent PEEM images of size $180 \mu\text{m} \times 130 \mu\text{m}$ are separated by equal intervals $\Delta t = 0.8$ s.

Figure 8a shows a family of PEEM intensity profiles taken along the dashed line (parallel to the $(1\bar{1}0)$ -direction) in Figure 7. The profiles corresponding to later moments are shifted in the vertical direction. The intensity increase during the collision is visible in the fifth profile from the bottom. Figure 8b displays the trajectories of the intensity maxima for the profiles presented in Figure 8a. We see that these trajectories do not simply pass one through another, which would have been expected if the waves did not interact. Instead, a temporary “bound state” has been formed, whose lifetime can be estimated from Figure 8b as approximately 2 s.

It should be noted that two-into-one and two-into-two collisions (i.e., the soliton-like behavior) are occasionally also observed for dark oxygen waves. However, in these cases, a surface defect could usually be seen located where collisions have taken place. This defect apparently modified the local properties of the surface.¹⁹

3. Modeling

3.1. The Kinetic Model. The modeling of the CO-oxidation reaction on Pt(110) is based on the decomposition of the entire reaction into elementary steps. These steps include processes of adsorption and desorption of molecules, the reaction and the structural phase transition. Independent studies of each of these processes have been previously conducted, yielding detailed data about their characteristic rates. In the model by Krischer and Eiswirth,^{16,17,49} the surface coverages of CO and oxygen and the fraction of surface reconstruction represent the basic

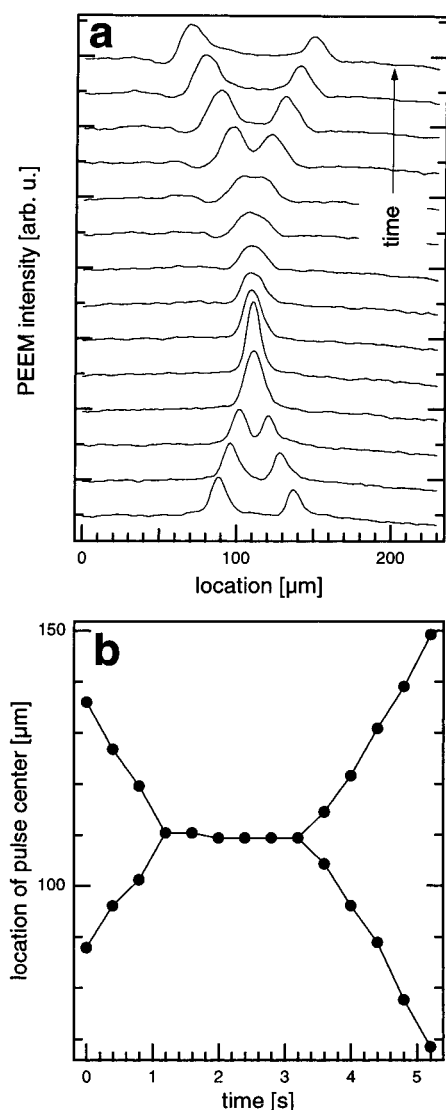


Figure 8. Spatial PEEM intensity profiles (a) and the respective time diagram (b) taken along the dashed line in Figure 7. Subsequent profiles, separated by equal intervals $\Delta t = 0.4$ s, are shifted upward to prevent their overlap. The time diagram (b) shows motion of the points corresponding to maximal PEEM intensity in the colliding pulses.

variables. Their temporal evolution is described by a set of differential equations, deduced from the experimental data.

We have recently extended this model to account for the observation of subsurface oxygen formation in island conversion experiments.⁴⁰ As an additional variable, this model includes the concentration of subsurface oxygen. Formation of subsurface oxygen from the surface oxygen species, and its back transformation are additional processes which are taken into account.

According to our previous analysis,⁴⁰ formation of subsurface oxygen takes place only on the nonreconstructed 1×1 surface. Hence, its rate is proportional to the local fraction of nonreconstructed area. Moreover, it is assumed in the model that subsurface oxygen atoms can occupy only a single level, lying directly under the surface. Therefore, the conversion rate is also proportional to the number of free sites in this layer.

An essential aspect of the extended model⁴⁰ is that subsurface oxygen influences the structure of the surface. Similar to adsorbed CO molecules, it favors lifting of the surface reconstruction (i.e., the 1×1 phase). Similar to the effect due to CO coverage in the original model, the influence of subsurface

oxygen becomes significant only at sufficiently high concentrations of subsurface oxygen.

Though the reverse process (i.e., the return of subsurface oxygen to the surface) has been included in the model,⁴⁰ it has been neglected in the numerical simulations, since no reliable estimates for this process could have been derived from the island conversion experiments analyzed in that study. However, it plays an important role under the reaction conditions and determines the collision properties of wave fragments, as shown below. Therefore, the explicit form of the respective term in the model equations is now significant. By comparing the profiles of simulated subsurface oxygen waves with the observed profiles of PEEM intensity, we have found that they are properly described under the assumption that the rate of back transformation is independent of the local CO coverage and depends only on the number of surface sites not covered with oxygen. Hence, in contrast to adsorption of oxygen from the gas phase, the CO molecules sitting on the surface do not prevent the return of oxygen to the surface from the subsurface level.

The following equations constitute the kinetic model used in our numerical simulations. Here the variable u denotes the local CO coverage, v represents the surface oxygen coverage, and s is the local concentration of subsurface oxygen; all these three properties can vary in the interval from 0 to 1. The variable w describes the local structural state of the surface. Its extreme values $w = 0$ and $w = 1$ correspond to the reconstructed 1×2 and nonreconstructed 1×1 phases, respectively. The intermediate values correspond to microscopic mixtures of both phase. Hence, this variable generally specifies the local fraction of the surface area found in the nonreconstructed phase. The equations are

$$\frac{\partial u}{\partial t} = k_1 p_{\text{CO}}(1 - u^3) - k_2 u - k_3 uv + D_x \frac{\partial^2 u}{\partial x^2} + D_y \frac{\partial^2 u}{\partial y^2} \quad (1)$$

$$\frac{\partial v}{\partial t} = k_4 p_{\text{O}_2} [s_{\text{O},1 \times 1} w + s_{\text{O},1 \times 2} (1 - w)] (1 - u - v)^2 - k_3 uv - k_6 vw(1 - s) + k_7 s(1 - v) \quad (2)$$

$$\frac{\partial w}{\partial t} = k_5 (f(u, s) - w) \quad (3)$$

$$\frac{\partial s}{\partial t} = k_6 vw(1 - s) - k_7 s(1 - v) \quad (4)$$

These equations contain various terms corresponding to different processes that affect the concentrations of reacting species and influence the state of the surface. The processes taken into account in eq 1 are adsorption of CO, its desorption, reaction of CO_{ad} with O_{ad} , and diffusion of adsorbed CO molecules on the surface. Equation 2 includes the terms corresponding to adsorption of oxygen, its reaction with CO_{ad} , formation of subsurface oxygen, and the back conversion. Equation 3 describes the dynamics of the phase transition variable, influenced by the CO coverage and by the concentration of subsurface oxygen. Equation 4 describes formation of subsurface oxygen from the surface oxygen species and its back conversion.

The function $f(u, s)$ in the eq 3 has the form

$$f(u, s) = \frac{\exp[(u - u_0)/\delta_u] + \exp[(s - s_0)/\delta_s]}{1 + \exp[(u - u_0)/\delta_u] + \exp[(s - s_0)/\delta_s]} \quad (5)$$

It describes the influence of CO coverage and concentration of subsurface oxygen on the structural state of the surface. The

TABLE 1

symbol	value	meaning
k_1	3.14×10^5 ML/s mbar	impingement rate constant of CO molecules
k_2	$= \nu_2 \exp(-E_2/k_B T)$	desorption rate constant of CO molecules
k_3	$\nu_2 = 2 \times 10^{16} \text{ s}^{-1}$ $E_2 = 38 \text{ kcal/mol}$ $= \nu_3 \exp(-E_3/k_B T)$ $\nu_3 = 3 \times 10^6 \text{ s}^{-1}$ $E_3 = 10 \text{ kcal/mol}$	reaction rate constant
k_4	5.86×10^5 ML/s mbar	impingement rate constant of O ₂ molecules
k_5	$= \nu_5 \exp(-E_5/k_B T)$ $\nu_5 = 7660 \text{ s}^{-1}$ $E_5 = 9.6 \text{ kcal/mol}$	rate constant of the phase transition
k_6	$= \nu_6 \exp(-E_6/k_B T)$	subsurface oxygen formation rate constant
k_7	$\nu_6 = 282 \text{ s}^{-1}$ $E_6 = 8.2 \text{ kcal/mol}$ $= \nu_7 \exp(-E_7/k_B T)$ $\nu_7 = 188 \text{ s}^{-1}$ $E_7 = 8.2 \text{ kcal/mol}$	rate constant of subsurface back conversion
$s_{0,1 \times 1}$	0.4	oxygen sticking coefficient on the 1 × 1 phase
$s_{0,1 \times 2}$	0.6	oxygen sticking coefficient on the 1 × 2 phase
u_0, δ_u	0.35, 0.05	parameters of function $f(u,s)$ for CO
s_0, δ_s	0.33, 0.08	parameters of function $f(u,s)$ for subsurface oxygen
$D_{x,y}$	$= D_{x,y}^0 \exp(-E_{x,y}/k_B T)$	diffusion coefficients for CO in x-direction (001) and y-direction (110)
	$D_x^0 = 7.5 \times 10^{-2} \text{ s}^{-1}$ $E_x = 12.3 \text{ kcal/mol}$ $D_y^0 = 4.3 \times 10^{-3} \text{ s}^{-1}$ $E_y = 12.3 \text{ kcal/mol}$	

parameters u_0 and s_0 determine the threshold values, above which the adsorbed CO molecules and subsurface oxygen are significantly affecting the surface structure. The parameters δ_u and δ_s specify how steep the respective thresholds are.

In our simulations the x -axis is always parallel to the (001)-direction and the y -axis is parallel to the orthogonal (110)-direction. The oxygen diffusion is very weak at considered temperatures and is therefore not included into the model. Generally, the diffusion constants of CO can depend on the CO coverage and the state of the surface (see ref 45). This effect is, however, not important for the processes considered in the present paper and is therefore not taken into account here. We also neglect a possible dependence of the rate constants for reaction and CO desorption on surface coverages.

In absence of subsurface oxygen, the model 1–5 reduces to the equations earlier used to describe wave propagation and spatio-temporal pattern formation in this reaction.^{16–19,33} We have employed basically the same parameter values for elementary processes in these equations as in the previous investigations. Improved numerical estimates for CO diffusion constants have, however, been now derived by an analysis of the available experimental data.⁴⁵

The additional model parameters, related to the processes involving subsurface oxygen, are k_6 , k_7 , s_0 , and δ_s . As discussed previously,⁴⁰ their values can be determined from oxygen island conversion measurements. We show in the next section that these experimental data allow to fix these parameters, yielding quantitative agreement between the theory and the experiments.

All model parameters, used in our numerical calculations, are listed in Table 1. Three parameters are absent from the

table since they can be varied in the experiment. These control parameters are the CO partial pressure p_{CO} , the oxygen partial pressure p_{O_2} , and the temperature T .

To compare simulations with the experimental data, yielded by PEEM, a relationship between the local PEEM image intensity and the model variables should be known. As discussed in the previous publications,⁴⁰ this intensity can be approximated by a linear weighted combination

$$i = -0.3u - v + 3s \quad (6)$$

of CO and O coverages and of the subsurface oxygen concentration. Note that adsorbed CO and O decrease the image intensity, whereas subsurface oxygen leads to a strong increase of the local brightness.

3.2. Island Conversion. In the Experimental Section we have emphasized that the phase transition should play an important role in the island conversion and provide a kind of memory to an island. We have also noted that the details of the island preparation are apparently important for its subsequent behavior. Since no subsurface oxygen is involved at the preparatory stage, when an surface oxygen island is grown, this process can be described by the reduced version of the model given by eqs 1–4. The basic parameters of this reduced model are known from previous studies,^{17,40} and we employed them in a numerical simulation of the preparatory stage.

For simulations we have used a grid of 200×400 points corresponding to a real size of $200 \mu\text{m} \times 400 \mu\text{m}$. The simulation of the preparation procedure started with the initial condition $u = 1$ everywhere, corresponding to a completely CO covered surface. The surface structure was initially set to $w = 1$, which is the 1×1 nonreconstructed state observed under a complete CO coverage. The initial control parameters were $T = 342 \text{ K}$, $p_{\text{CO}} = 0$, and $p_{\text{O}_2} = 2 \times 10^{-5} \text{ mbar}$.

A small perturbation ($u = 0$ locally) was then placed in the middle of the system, allowing oxygen to adsorb. Adsorption of oxygen into the perturbed area created a small oxygen island that started to grow because of the CO diffusion and further oxygen adsorption on the vacant sites. After $\Delta t = 420 \text{ s}$, the island has reached a horizontal extension of $240 \mu\text{m}$.

During the following heating stage the temperature was stepwise increased by 30 K every 6 s until it reached the values of 400, 453, or 503 K. This represents an average heating rate of 5 K/s. We have checked that employing smaller temperature steps did not significantly affect the distributions of the variables at the end of the heating stage.

The most interesting result of this simulation is the behavior of the phase transition variable w inside the growing island. Figure 9 shows vertical w -profiles through the island of the whole experiment, including growth, heating, and the final conversion. We see that at the end of the preparatory stage a significant fraction of the surface area in the periphery of the island is still found in the nonreconstructed 1×1 phase, corresponding to nonvanishing values of w . This happens because CO molecules have only very recently left this area and, since the phase transition is slow, the local state of the surface has not yet adjusted to their absence. In contrast to this, the values of w in the middle of the island are much lower, since more time has passed here after the disappearance of CO molecules from the surface. As follows from eq 4, the oxygen conversion rate is proportional to w . Hence, faster initial conversion to subsurface oxygen can indeed be expected in the periphery of the islands, in agreement with the experimental data.

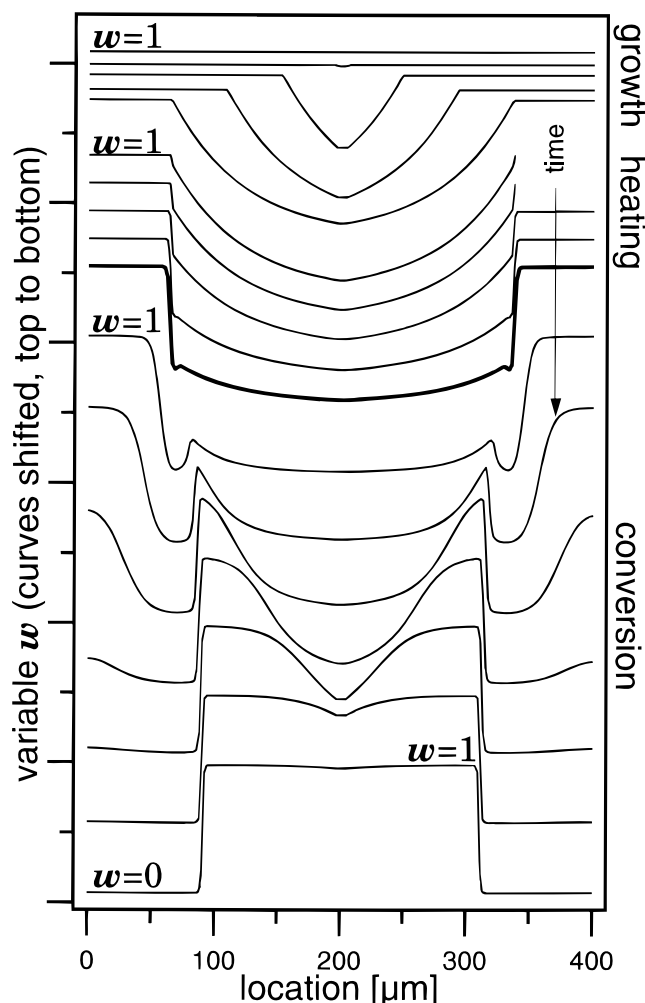


Figure 9. Calculated spatial profiles of the phase transition variable w during growth of an island, the heating stage, and subsequent island conversion. The model parameters are the same as in Figure 12b, the vertical cross-section through the center of the larger island in Figure 12b is chosen. The profiles at subsequent moments $t = 0, 60, 66, 200, 340, 480, 484, 488, 492, 496, 500, 530, 560, 590, 620, 650, 680, 720$ s are shifted downward to prevent their overlap.

To quantitatively describe the subsequent stage, involving formation of subsurface oxygen and its return to the surface, the rate constants in the eq 4 and the parameters of the function 5 should be known. In our previous publication⁴⁰ we have obtained some estimates of these parameters, based on the comparison between simulations of the island conversion and the experimental measurements. However, these estimates were not very precise, since the reverse process (i.e., the return of subsurface oxygen to the surface) had been neglected. Moreover, the amount of available experimental data was not large enough. Since the experiments on island conversion have now been repeated under controlled conditions for different temperatures, as described in section 2.2, their data can be used to obtain improved estimates for these parameters.

The conversion experiments of surface oxygen islands to subsurface oxygen are better suited to extract the conversion rate constants than the experiments under continuous reaction conditions. Indeed, during the conversion stage, CO is absent. Hence, we can eliminate from the model all terms involving the CO coverage u . Note that since CO is the only diffusing species in the model, its absence implies that the conversion processes in different parts of the island proceed independently

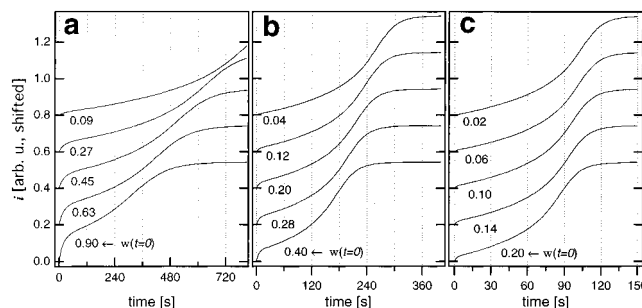


Figure 10. Computed temporal profiles of the PEEM intensity at selected spatial locations at different temperatures (a) $T = 400$ K, (b) $T = 453$ K, and (c) $T = 503$ K.

and the difference between them is explained only by the difference in the respective initial conditions.

The local conversion process is then described by a set of only two ordinary differential equations

$$\frac{dw}{dt} = k_5(f^*(s) - w) \quad (7)$$

$$\frac{ds}{dt} = k_6w(1-s)^2 - k_7s^2 \quad (8)$$

where

$$f^*(s) = \frac{1}{1 + \exp[(s_0 - s)/\delta_s]} \quad (9)$$

In the second of these equations we have taken into account that, in absence of the reaction, the total amount $v + s$ of surface and subsurface oxygen is locally conserved. Since initially, at the end of the preparatory stage, we have $v = 1$ and $s = 0$ inside the island, the relation $v = 1 - s$ holds. The differential equations can be integrated for different initial conditions using standard numerical methods.

In the Experimental Section we have constructed curves (Figure 2) of the local island conversion process, based on subsequent local measurements of the PEEM intensity at several temperatures. They show the progress of the island conversion at several selected locations. By numerically integrating eqs 7 and 8 with appropriate initial conditions, the conversion processes at various locations can be reproduced. Looking again at the profiles of Figure 9, we see that at the end of the preparatory stage different values of w are established at different locations inside the island. We take initial values of w , that approximately correspond to the values of this variable found at the respective locations. The computed conversion curves are shown in Figure 10, where the initial values of w are also given. These curves can now be compared with the respective experimental curves in Figure 2.

We see that both sets of curves show satisfactory agreement. Not only the characteristic conversion times and time shifts for the conversion in the middle and in the periphery of an island are correctly reproduced, but even the shapes of the curves are quite similar. A qualitative difference is seen only at temperature $T = 400$ K (Figures 2a and 10a). It is, however, explained, if we notice that in the experiment the island was quickly shrinking with time at this temperature, because of the residual CO coverage on the surface. This effect has not been taken into account in the above theoretical calculations, based on eqs 7 and 8. But even in this case the theoretical curves yield reasonable agreement for the conversion times in the central part of the island (i.e., in the area not affected by its shrinking).

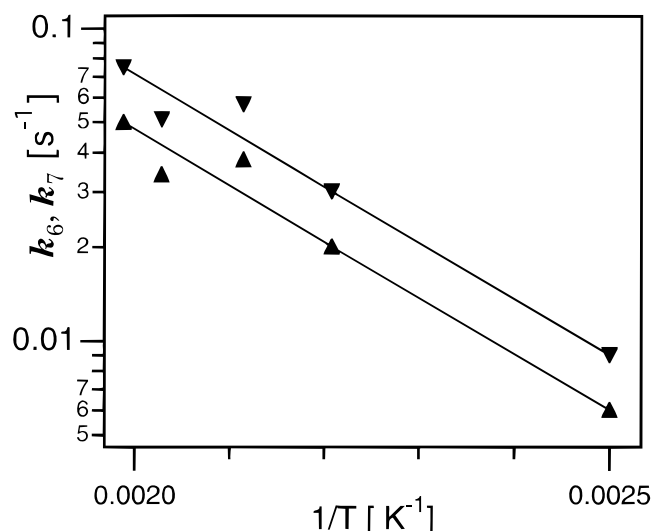


Figure 11. Arrhenius plots of the oxygen conversion rates; the values of $\log k_6$ (▼) and $\log k_7$ (▲) are plotted as functions of $1/T$. The straight lines represent the best linear fits of these dependences.

This fitting of the conversion curves has been performed for five different temperatures of $T = 400, 453, 473, 493$, and 503 K. At all these temperatures, a satisfactory agreement has been obtained using the same parameters $s_0 = 0.33$ and $\delta_s = 0.08$ in the function given by eq 9. The obtained values of the oxygen conversion rate constants k_6 and k_7 depended, however, on temperature.

We have analyzed the temperature dependence of the conversion rate constants. If these rate constants obey the Arrhenius activation law, i.e.

$$k_6 = \nu_6 \exp\left(-\frac{E_6}{k_B T}\right), \quad k_7 = \nu_7 \exp\left(-\frac{E_7}{k_B T}\right) \quad (10)$$

the dependence of $\ln k_6$ and $\ln k_7$ on the inverse temperature should be linear. In Figure 11 the obtained values of these rate constants are plotted in the logarithmic scale as function of the inverse temperature. We see that for both processes the rate constants approximately follow the Arrhenius law. Using the linear fitting, we have thus deduced the activation energies $E_6 = E_7 = 8.2 \pm 1$ kcal/mol. The preexponential factors of the forward and backward oxygen conversion rates are estimated as lying inside the intervals $\nu_6 = 127\text{--}628 \text{ s}^{-1}$ and $\nu_7 = 84\text{--}418 \text{ s}^{-1}$ with the mean values $\nu_6 = 282 \text{ s}^{-1}$ and $\nu_7 = 188 \text{ s}^{-1}$ (the asymmetry of mean value and error interval resulting from the fit on the logarithmic axis).

Thus, the model parameters related to subsurface oxygen have been fixed by analyzing the conversion process described by the reduced eqs 7 and 8. Now, when these parameters are known, the two-dimensional numerical simulations of the full model, given by eqs 1–4, can be resumed to reproduce the properties of the island conversion observed in the experiments. We return to the two-dimensional distributions, obtained at the end of the preparatory stage, and integrate further the full model equations. Note that, since the accompanying time evolution of CO coverage is also computed, we would thus also take into account possible effects of the residual CO coverage, leading to more or less pronounced shrinking of the islands.

To compare the computation results with the experimental data, we have constructed, using eq 6, the PEEM images that would correspond to the computed distributions. Figure 12 shows sequences of thus generated PEEM images at three different temperatures. They should be compared with the

respective experimental images displayed in Figure 1. The subsequent frames in Figure 12 are separated by the same time intervals and have the same sizes as in Figure 1. We see that the simulations yield not only qualitative, but also a satisfactory quantitative agreement with the experiments for the entire conversion process.

At the lower temperature $T = 400$ K (Figures 1a and 12a), the conversion begins in a narrow fringe at the island boundary, that spreads toward the center. This is accompanied by rapid shrinking of the island, since, at this temperature, CO has not completely desorbed after heating from the surface. We can also see that, as in the experimental images, the area left behind the retreating island has a slightly higher PEEM intensity since the surface is almost clean there.

To reproduce the experimental situation at $T = 453$ K, displayed in Figure 1b, where two islands of different sizes are present, we have created in the simulation an additional small island. This has been done by applying during the preparatory stage, in addition to the first perturbation at $t = 0$, another perturbation at a later moment $t = 200$ s and thus creating a second smaller oxygen island. We see in Figure 12b that, similar to the experiment, the conversion of the smaller island proceeds faster and is already completed between frames 4 and 5.

At the higher temperature $T = 503$ K the simulations show more homogeneous conversion (Figure 12c), similar to the experimental data (Figure 1c).

Hence, the experimental PEEM images, taken during the island conversion process, can be satisfactorily reproduced in the numerical simulations. But, in contrast to PEEM experiments where only a combination of oxygen and CO coverages and of the subsurface oxygen concentration is imaged, the simulations yield detailed information about spatial distributions of all these species and the local structural state of the surface during the entire conversion process.

As an example, we show in Figure 9 the profiles of the phase transition variable w at subsequent time moments during growth of the island, its heating, and the following conversion. We have earlier discussed the upper profiles in this figure that correspond to the preparatory stage. These profiles are plotted along a vertical cross-section through the larger island in Figure 12b. The top profile with $w = 1$ displays the initial situation before the perturbation is applied. As the island grows, the variable w drops where CO is absent, thus forming a bowl-like distribution. During the heating interval, this distribution is uniformly reduced over the entire profile. At the end of heating, the starting distribution of w for the conversion process is generated (it is shown by a thick curve in Figure 9). During the conversion stage, the variable w increases and reaches the value close to 1 in those parts of the island, where conversion to the subsurface oxygen has already taken place. This is a consequence of the influence of subsurface oxygen that tends to stabilize the nonreconstructed phase, similar to the action of the adsorbed CO molecules.

Heating to a higher temperature yields a more flat w distribution at the end of the preparatory stage. Therefore, the conversion proceeds more uniformly at these temperatures, as indeed seen in Figures 1 and 12.

The previous results from island conversion simulations can be used to rationalize the behavior found when exposing a converted subsurface oxygen island to CO. As follows from the above simulations, the fully converted island consists not only of subsurface oxygen. Indeed, because of the back conversion process, some surface oxygen is also present there.

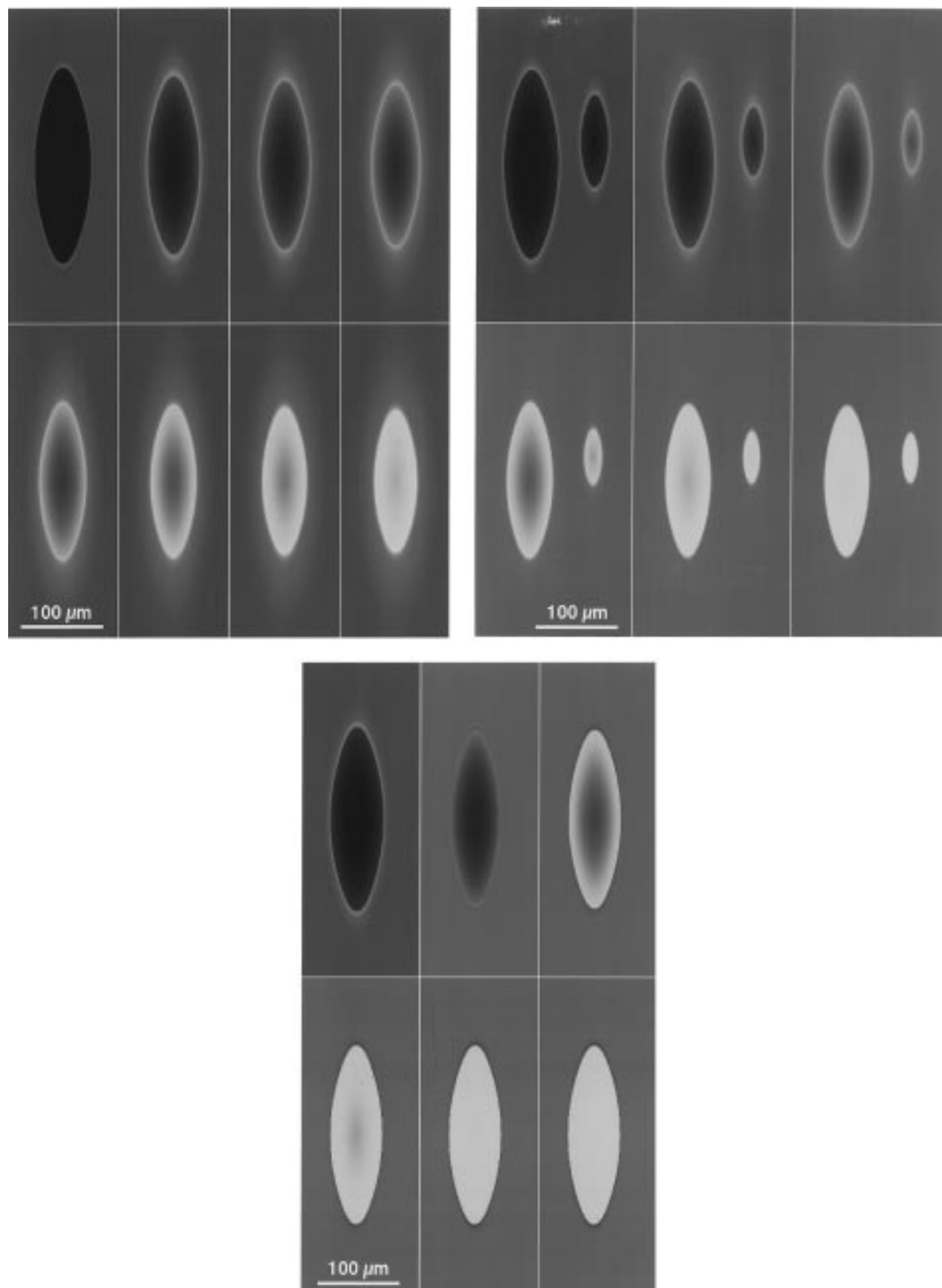


Figure 12. Conversion of oxygen islands at temperatures (a) $T = 400$ K, (b) $T = 453$ K, and (c) $T = 503$ K. Subsequent computed PEEM images are separated by equal time intervals Δt and shown from top left to bottom right. The parameters are (a) $\Delta t = 120$ s, image size $140 \mu\text{m} \times 400 \mu\text{m}$; (b) $\Delta t = 60$ s, $200 \mu\text{m} \times 400 \mu\text{m}$; and (c) $\Delta t = 30$ s, $150 \mu\text{m} \times 400 \mu\text{m}$.

The equilibrium between the two species is determined by the ratio of the rate constants k_6 and k_7 . When CO molecules arrive

at the surface, they react with the adsorbed oxygen from the island. Thus, O_{ad} is quickly removed from the island area and

only subsurface oxygen remains there. As can be seen in eq 6, the contribution from adsorbed oxygen, responsible for a lower PEEM intensity, will be absent then and the intensity level of pure subsurface oxygen becomes visible. The almost instant removal of surface oxygen allows further subsurface oxygen to come onto the surface, which finally leads to the total disappearance of the island.

3.3. Subsurface Oxygen Waves. The model, given by eqs 1–4, yields quantitative description of the experiments on oxygen island conversion at different temperatures. In the next sections we show that the same model reproduces as well the behavior observed under reaction conditions (i.e., under permanent supply of CO molecules). The questions to be addressed here are whether the model yields both oxygen and subsurface oxygen waves and correctly describes their collision properties.

Before we proceed to detailed simulations of traveling reaction waves, it should be noted that a detailed quantitative agreement with the experiments is not expected here. Indeed, our model represents an extension of the previous model by Krischer and Eiswirth^{16,17} and reduces to it when production of subsurface oxygen is negligible (i.e., for the traveling oxygen pulses). However, though the Krischer–Eiswirth model correctly describes the general structure of the bifurcation diagram for this system, the boundaries determining bistable, excitable, and oscillatory regions in this diagram are shifted with respect to the parameter values, under which these regimes are observed in the experiments. Therefore, traveling oxygen pulses have been found in the earlier simulations^{18,19} only in the parameter region that does not fit to the experimental data.

Apparently, the main source of this remaining discrepancy lies in the possible dependence of the desorption rate constant of CO and of the reaction rate constants on the adsorbate coverages. Indeed, it is known that relatively strong interactions between CO molecules on Pt are present^{50,51} and they can lead to such dependences. It has been shown³⁷ that, by introducing coverage dependence of the desorption and reaction rate constants into the model, its bifurcation diagram can be brought closer to the experimental data. A possible effect of the coverage dependence on the properties of traveling reaction waves has, so far, not been analyzed. Our attention in the present study is focused on the phenomena related to the formation of subsurface oxygen in the considered reaction. Therefore, we have not attempted here to take into account interactions between the reacting molecules. At present, no reliable experimental data on the coverage dependence of the reaction rate due to such interactions under standard reaction conditions is available.

Moreover, as already noted above in the experimental part, bright traveling waves corresponding to formation of subsurface oxygen have usually been found in the experiments after several cycles of oxygen island conversion were performed on the same crystal. The repeated island conversion experiments might lead to a long-term modification of the surface properties due to roughening or facetting.⁵² We cannot exclude also another possibility that oxygen penetrates into the bulk of the crystal and is slowly accumulated there. Furthermore, traveling subsurface waves are typically found at temperatures that are significantly higher than the temperatures at which the experiments on island conversion are performed. Therefore, conversion rate constants and other parameters deduced from such experiments should be extrapolated to higher temperatures in order to simulate these traveling waves. Hence, we expect that our model would generally yield only qualitative agreement with the experiments for the traveling reaction waves.

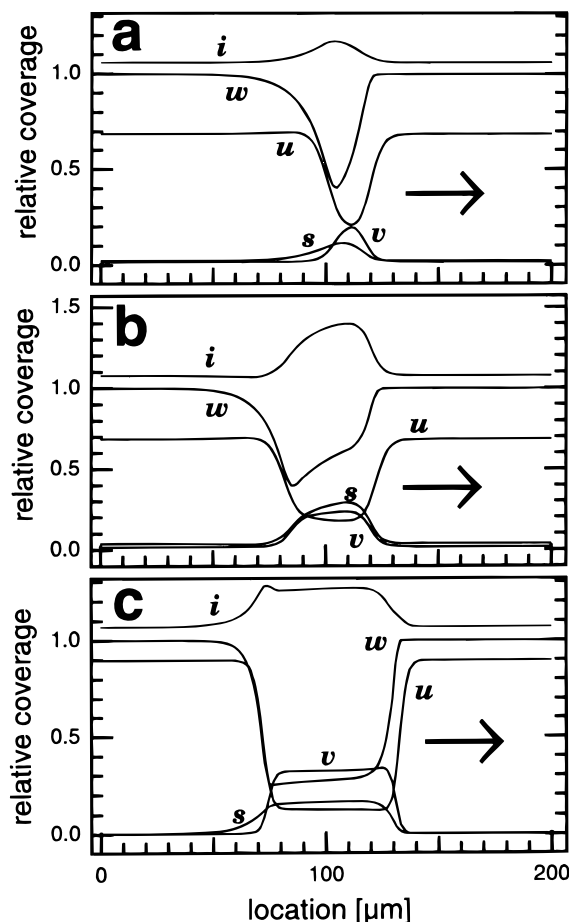


Figure 13. Spatial profiles of traveling subsurface oxygen pulses for the parameters (a) $T = 541$ K, $p_{\text{CO}} = 4.14 \times 10^{-5}$ mbar, $p_{\text{O}_2} = 1.1 \times 10^{-4}$ mbar, $k_6 = 1.23$ s $^{-1}$, $k_7 = 0.82$ s $^{-1}$; (b) $T = 541$ K, $p_{\text{CO}} = 4.14 \times 10^{-5}$ mbar, $p_{\text{O}_2} = 1.1 \times 10^{-4}$ mbar, $k_6 = 9$ s $^{-1}$, $k_7 = 4$ s $^{-1}$, $s_0 = 0.275$; and (c) $T = 523$ K, $p_{\text{CO}} = 2.84 \times 10^{-5}$ mbar, $p_{\text{O}_2} = 1.1 \times 10^{-4}$ mbar, $k_6 = 0.6$ s $^{-1}$, $k_7 = 0.4$ s $^{-1}$, $s_0 = 0.246$. Other model parameters are given in Table 1.

When simulations of the traveling waves, using the parameters taken from Table 1, have been performed, only negligible small amounts of subsurface oxygen were found to accompany a traveling pulse. These small amounts did not change the intensity of PEEM images for such waves and their collision properties. Such structures represented the usual traveling oxygen waves that are well described by the earlier models.^{18,19}

To obtain in our simulations the traveling bright waves, higher values of the conversion rate constants k_6 and k_7 have to be taken into account (though in the case of complex bistability these values were still lying within the accuracy limits of our numerical estimates based on the island conversion data). Moreover, we had to slightly decrease the threshold s_0 in function 5 thus making the surface structure more sensitive to the presence of subsurface oxygen. When the simulation parameters were different from the values, given in Table 1, their numerical values are given in the figure captions.

Figure 13 shows three different subsurface oxygen pulses. The pulses, displayed in Figure 13a,b, correspond to the excitable state of the system, while the pulse shown in Figure 13c is found in the parameter region of complex bistability. For all of them, the spatial profile of the simulated PEEM intensity i shows a local increase in the pulse region, i.e., these waves are bright.

Though the pulse, presented in Figure 13a is already slightly brighter than the surrounding surface, the amount of subsurface

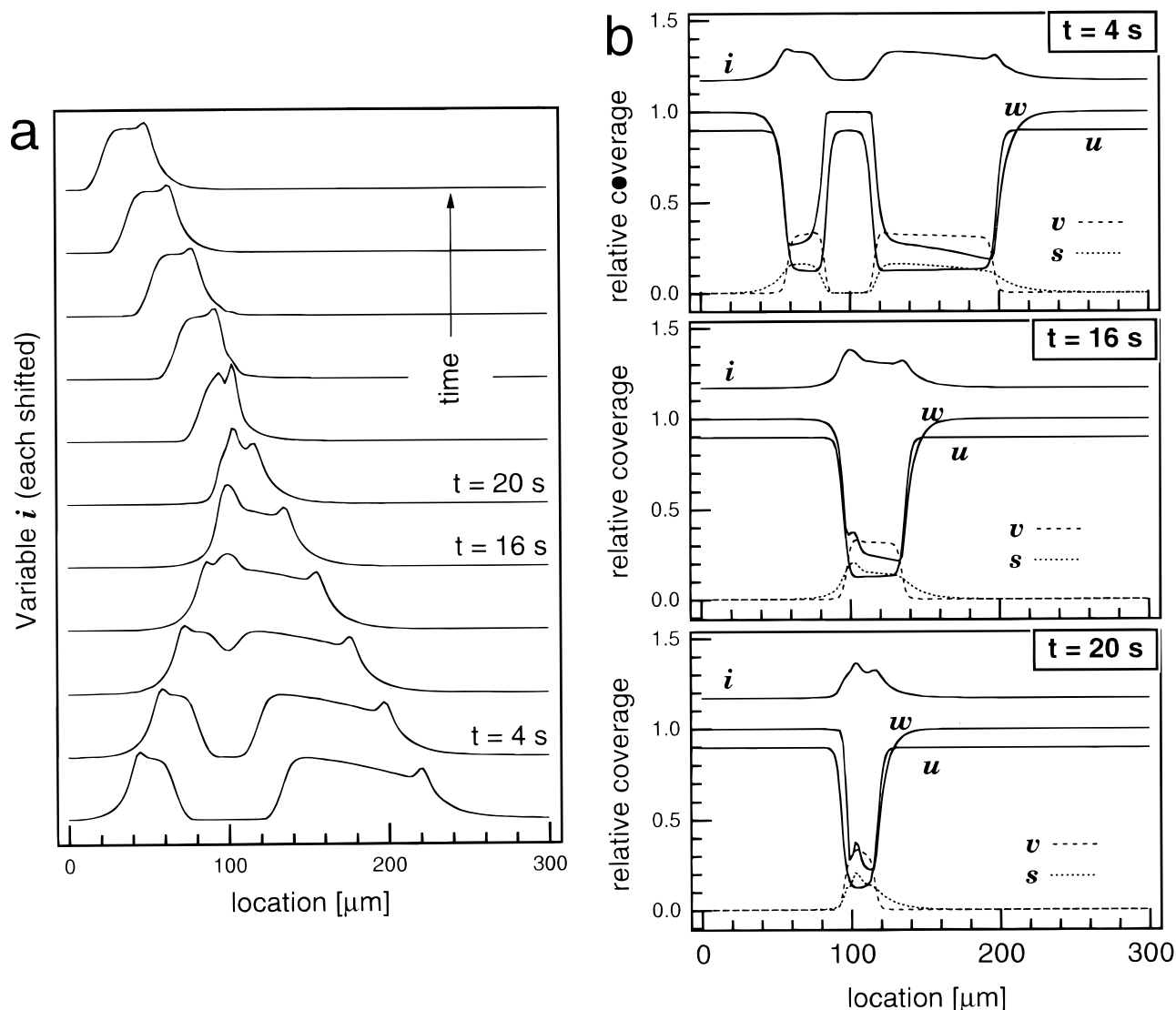


Figure 14. Spatial profiles of PEEM intensity (a) during a two-into-one collision. For three selected moments profiles of all variables are shown (b). The same parameters as in Figure 13c are used, the time interval between subsequent profiles is $\Delta t = 4$ s.

oxygen traveling with this pulse remains relatively low and its effect on the profiles of CO and oxygen coverages in the pulse, as well as on the profile of the phase transition variable w inside it, is weak. Our numerical simulations of frontal collisions between two such pulses show that they always annihilate in the same way as two dark oxygen pulses.

The traveling subsurface oxygen pulse, presented in Figure 13b, has been obtained by choosing a higher rate constant for subsurface oxygen formation and a lower value of s_0 while keeping all other parameters the same as in Figure 13a. We see that this change leads to an increase in the amount of subsurface oxygen in the pulse. Subsurface oxygen already affects in this case the phase transition leading to a deformation of the w -profile. Moreover, the pulse becomes wider and propagates slower. While the pulse velocity was $11 \mu\text{m/s}$ in Figure 13a, it is reduced to $9.6 \mu\text{m/s}$ in Figure 13b. Collisions of two such pulses do not result in annihilation. Instead, reflections events are here observed in the simulations, as will be discussed in detail in section 3.5.

Figure 13c shows a subsurface oxygen pulse in the regime of complex bistability. In this case the system has two stationary states that correspond to the predominantly CO-covered and oxygen-covered surfaces. Two different kinds of traveling

fronts, corresponding to transitions between these two states, are present in the system. Though generally the velocities of such fronts are different, they become close in some parameter regions. The pulse shown in Figure 13c is a combination of two opposite fronts moving one after another at almost equal velocities near to $4 \mu\text{m/s}$. Collisions between two such pulses of different widths are considered in the next section.

3.4. Two-into-One Collisions. Figure 14 presents a simulation of two colliding pulses in the bistable kinetic regime of the reaction. The pulses propagate along the $(1\bar{1}0)$ -direction. To produce the pulses, the surface was initially set in the CO covered state. The left pulse was initiated by setting the left boundary temporarily into the oxygen covered state, thus releasing an oxygen front. The rear part of the pulse was then generated by setting the left boundary back to the CO covered state. On the right side the same procedure was performed, except that more time was allowed to pass between triggering the oxygen front and the subsequent CO front. Therefore, the right pulse is significantly wider. Since the propagation velocities of fronts are very close in this case, the width of each pulse is approximately preserved after its generation. Figure 14a shows the calculated PEEM intensities of both pulses, as they move toward each other and then collide. Figure 14b

displays the respective spatial distributions for all involved species at three subsequent time moments.

At time $t = 4$ s in Figure 14b, both pulses are seen traveling before the collision. The profile of the CO coverage u is always slightly advanced with respect to the profile of the phase transition variable w along the propagation direction. At time $t = 16$ s both oxygen fronts have already merged. The oxygen-covered region in the middle is bounded by two CO fronts that are moving toward one another. Note, however, that the profiles are not symmetrical. Both the oxygen coverage v and the subsurface oxygen concentration s are slightly increased at $x = 100$ μm . This happens because at this location the two propagating oxygen fronts have collided shortly before and more subsurface oxygen has been formed here.

This small modification is sufficient to change the outcome of the collision. As seen at time $t = 20$ s in Figure 14b, when the left colliding CO front reaches the location at which an increased amount of subsurface oxygen is present, it changes its direction and is transformed into an oxygen front moving in the left direction. When the right CO front later reaches the same location, the local concentration of subsurface oxygen in this area would already so much diminish that no analogous transformation occurs with this second front and it retains its shape and its direction of motion. Thus, a single pulse traveling in the left direction emerges as a result of the collision.

The subsequent profiles of PEEM intensity, obtained in this simulation (Figure 14a), are qualitatively similar to the experimental data shown in Figure 6a. We did not try to exactly reproduce the experimentally observed collision, because of the model limitations that have been discussed in the previous section. However, the values of the conversion rate constants $k_6 = 0.6$ s^{-1} and $k_7 = 0.4$ s^{-1} , used in this simulation at $T = 523$ K, were obtained by applying the Arrhenius dependences (eq 10) with the activation energies $E_6 = E_7 = 7.2$ kcal/mol and the prefactors $\nu_6 = 628$ s^{-1} , $\nu_7 = 418$ s^{-1} . These activation energies and prefactors correspond to the highest estimates for k_6 and k_7 as derived in section 3.2 by the analysis of island conversion experiments. Hence, our analysis of the island conversion phenomena is consistent with the results of experiments on two-into-one collisions of subsurface oxygen waves; it yields numerical estimates of the model parameters, related to subsurface oxygen, that remain meaningful also under the reaction conditions at higher temperatures.

3.5. Two-into-Two Collisions. In this section we reproduce, using the model given by eqs 1–4, the collision behavior of subsurface oxygen waves described in section 2.5. As already noted, the collisions between bright wave fragments resulting in reflection are relatively rare. Moreover, whenever they are observed, all fragments traveling in the same direction seem to have the same thickness. This suggests that the reaction forms an excitable system in this kinetic regime, where the width of traveling pulses is uniquely determined by the system parameters (see ref 53). We have further observed in section 2.5 that the reflections occur only for frontal collisions of the fragments moving along the x -direction. All other collisions lead to annihilation of colliding waves.

Figure 15 presents the calculated profiles of the PEEM intensity for a collision of two identical pulses shown in Figure 13b. We see that they reproduce qualitatively well the respective experimental behavior in Figure 8a. As the pulses collide, the local PEEM intensity increases, reflecting the increased value of subsurface oxygen coverage in the collision region. A metastable stationary bright object is formed at a location where the collision has taken place. After a while, this metastable

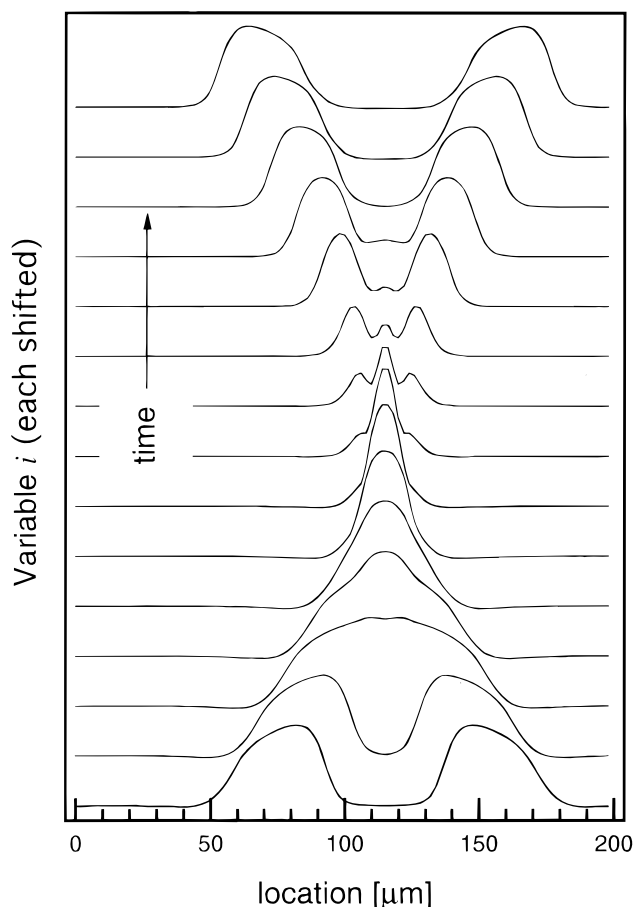


Figure 15. Spatial profiles of PEEM intensity during a two-into-two collision. The same parameters as in Figure 13b; the time interval between subsequent profiles is $\Delta t = 1$ s.

object disappears, simultaneously giving rise to two new pulses that run in the opposite directions out of the collision region. Effectively, the entire event can be thus described as a reflective collision.

To explain the observed behavior of colliding pulses, we note that, under the parameter values chosen in this simulation, the system was already very close to a situation where, in addition to the uniform stationary CO-dominated state, it would have another stationary state. This second stationary state corresponds to a high concentration of subsurface oxygen. It is possible because subsurface oxygen, present in sufficiently large amounts, plays a role similar to CO and stabilizes the nonreconstructed state ($w = 1$) of the surface. The bright object formed during the collision can be viewed as a temporarily existing domain of the other reaction state. Since this state is weakly unstable, the domain cannot be stationary and eventually disappears generating two traveling pulses.

Figure 16 shows results of a two-dimensional simulation, where two colliding bright fragments had different sizes and were only partially overlapping. The formation of a bright object in the collision region is clearly seen in frame 2 in this figure. In the next frame, this object already starts to die, simultaneously generating two small curved wave fragments. Later on, the bright object disappears while the two new fragments continue their motion (frames 4 and 5). Note that since the upper colliding fragment was longer, a small part on the left side of it has not undergone a collision. It continues to move in the original direction, merging with one of the secondary wave fragments generated in the collision zone.

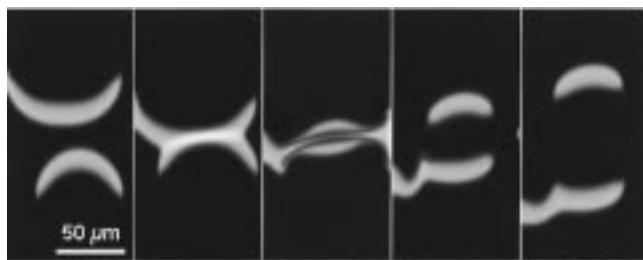


Figure 16. Simulation of a complex reflective collision in two dimensions. Subsequent computed PEEM images of size $100\ \mu\text{m} \times 200\ \mu\text{m}$ are separated by equal intervals $\Delta t = 4\ \text{s}$. The parameters are $T = 541\ \text{K}$, $p_{\text{CO}} = 4.15 \times 10^{-5}\ \text{mbar}$, $p_{\text{O}_2} = 1.1 \times 10^{-4}\ \text{mbar}$, $k_6 = 9\ \text{s}^{-1}$, $k_7 = 4\ \text{s}^{-1}$, $s_0 = 0.270$. Other model parameters are given in Table 1.

4. Discussion and Conclusions

New experimental data and the results of mathematical modeling, reported in this paper, confirm the earlier proposed mechanism of subsurface oxygen formation on the Pt(110) surface in the course of interaction with CO and O₂ and the influence exercised by subsurface oxygen on the surface phase transition. As follows from the analysis and modeling of oxygen island conversion experiments, formation of subsurface oxygen is taking place only on the nonreconstructed 1×1 surface and, in return, subsurface oxygen tends to stabilize this nonreconstructed surface phase, thus playing a role similar to that of CO adsorbate.

On the basis of the data of island conversion experiments at different temperatures, we have shown that the rate constants for forward and back conversion processes can well be described by the Arrhenius law. The estimates for the activation energies and preexponential factors for these two processes are obtained.

We have found that our model yields satisfactory quantitative agreement with the experimental data on island conversion. All experimental stages (i.e., growth of islands and their changes during heating, as well as the subsequent formation of subsurface oxygen), are correctly reproduced. The computed profiles of PEEM intensity show good agreement with the experimental images. The characteristic conversion times and the entire dynamical picture of the conversion process are correctly described by the model.

The experiments performed under reaction conditions, i.e., with the continuous supply of CO and O₂, have shown the existence of new spatio-temporal patterns in the considered reaction. These patterns include traveling bright waves and wave fragments. The properties of such observed patterns are different from those of normal (i.e., dark) traveling oxygen waves. Instead of complete annihilation, typical for oxygen (O_{ad}) waves, the two-into-one wave collisions are characteristic for traveling bright waves. Moreover, reflective two-into-two collisions between bright wave fragments have also been observed under different experimental conditions.

The kinetic model, developed on the basis of nonreactive island conversion experiments, is able to describe these new patterns. They correspond to traveling oxygen waves, whose propagation is accompanied by significant formation of subsurface oxygen. Moreover, the model explains special collision properties of bright waves by an increased temporary production of subsurface oxygen in the collision zone. The additional subsurface oxygen, pumped under the surface in the collision region, is then slowly released back to the surface. In the case of a reflective two-into-two collision, it later triggers two new pulses, running away in opposite directions from the collision region. For the two-into-one collisions, the returning oxygen

leads to a front transformation responsible for the emergence of a single pulse after the collision.

The computed PEEM intensity profiles for the two different collision processes are in qualitative agreement with the experimental data. They show a temporary increase of the PEEM intensity in the collision zone, corresponding to a higher subsurface oxygen level in this region.

Hence, the role of the subsurface species in wave collisions can be understood as providing a temporary storage capacity for oxygen. It can go below the surface, become temporarily stored there and later return, triggering new pulses or changing the propagation properties of the reaction fronts.

Though the reflective collisions are also possible⁵⁴ in simple two-component models, they represent there rather an exception and are observed only in the vicinity of special bifurcation points. The reflective collisions of dark (oxygen) traveling fragments in the CO oxidation reaction, which have been sometimes observed in the experiments, could have so far been clearly linked to the presence of surface defects in the collision region.¹⁹

Such effects are however generally expected in the three-component reaction–diffusion models, where an activator–inhibitor subsystem is enlarged by an additional reactive component.⁵⁵ Our analysis of the experimental situation reveals that the collision properties of bright traveling waves in the CO oxidation reaction on Pt(110) are intimately related to production of subsurface oxygen. The observed effects belong to a typical class of behavior of wave patterns in the extended activator–inhibitor systems.

In contrast to the oxygen island conversion phenomena, where satisfactory quantitative agreement between modeling and experiments has been reached, we have so far been able to only qualitatively reproduce the behavior and properties of wave patterns found in this system under reaction conditions. The values of the control parameters (i.e., of the partial pressures and temperature) had to be chosen differently in the simulations. Moreover, we had to significantly increase the rate constants of forward and back oxygen conversion processes to account for the appearance of traveling oxygen waves (though in the case of two-into-one collisions the used rate constants were still lying within the extrapolation limits).

Hence, the model needs further improvements, if complete quantitative agreement with the experimental data is aimed. Its extensions are possible in various directions. The coverage dependence of reaction and CO desorption rate constants can be incorporated into the model. There is also experimental evidence that adsorbed oxygen may form two surface species with different physical and reaction properties.^{5,6} Moreover, oxygen can perhaps form several subsurface levels or even go deeper into the bulk (these processes are indeed known for other metals, such as Pd, Rh,⁵⁶ Cu, or Ag⁵⁷).

Another possibility cannot yet be excluded that adsorbed CO molecules can locally, in a small neighborhood, modify the surface structure thus allowing oxygen atoms to go under the surface even if it is mainly found in the reconstructed 1×2 state. Furthermore, proper attention should be paid to the experimental observation that bright traveling fragments are typically observed on the surface after several island conversion cycles had been performed on it. This may indicate that some form of surface modification, such as roughening, is needed to create the conditions under which such patterns develop. These questions remain open and should be further investigated.

Acknowledgment. The authors are grateful to A. Preusser for his help in developing the “Virtual Laboratory” computation platform that has been employed in these simulations.

References and Notes

- (1) Ertl, G. *Surf. Sci.* **1994**, 299/300, 742.
- (2) Imbihl, R.; Ertl, G. *Chem. Rev.* **1995**, 95, 697.
- (3) Rotermund, H. H. *Surf. Sci. Rep.* **1997**, 29(7/8), 265.
- (4) Engel, T.; Ertl, G. *Adv. Catal.* **1979**, 28, 1.
- (5) Freyer, N.; Kiskinova, M.; Pirug, G.; Bonzel, H. P. *Surf. Sci.* **1986**, 166, 206.
- (6) Wilf, M.; Dawson, P. T. *Surf. Sci.* **1977**, 65, 399.
- (7) Ducros, R.; Merrill, R. P. *Surf. Sci.* **1976**, 55, 227.
- (8) Jackman, T. E.; Davies, J. A.; Jackson, D. P.; Unertl, W. N.; Norton, P. R. *Surf. Sci.* **1982**, 120, 389.
- (9) Comrie, C. M.; Weinberg, W. H.; Lambert, R. M. *Surf. Sci.* **1976**, 57, 619.
- (10) Wartnaby, C. E.; Stuck, A.; Yeo, Y. Y.; King, D. A. *J. Phys. Chem.* **1996**, 100, 12483.
- (11) McCabe, R. W.; Schmidt, L. D. *Surf. Sci.* **1976**, 60, 85.
- (12) Ertl, G.; Norton, P. R.; Rüstig, J. *Phys. Rev. Lett.* **1982**, 49, 177.
- (13) Gritsch, T.; Coulman, D.; Behm, R. J.; Ertl, G. *Appl. Phys. A* **1989**, 49, 403.
- (14) Gritsch, T.; Coulman, D.; Behm, R. J.; Ertl, G. *Phys. Rev. Lett.* **1989**, 63, 1086.
- (15) Imbihl, R.; Ladas, S.; Ertl, G. *Surf. Sci.* **1988**, 206, L903.
- (16) Eiswirth, R. M.; Krischer, K.; Ertl, G. *Appl. Phys. A* **1990**, 51, 79.
- (17) Krischer, K.; Eiswirth, M.; Ertl, G. *J. Chem. Phys.* **1992**, 96, 9161.
- (18) Bär, M.; Falcke, M.; Zülicke, C.; Engel, H.; Eiswirth, M.; Ertl, G. *Surf. Sci.* **1992**, 269/270, 471.
- (19) Bär, M.; Eiswirth, M.; Rotermund, H. H.; Ertl, G. *Phys. Rev. Lett.* **1992**, 69/6, 945.
- (20) Bär, M.; Gottschalk, N.; Eiswirth, M.; Ertl, G. *J. Chem. Phys.* **1994**, 100, 1202.
- (21) Bär, M.; Nettesheim, S.; Rotermund, H. H.; Eiswirth, M.; Ertl, G. *Phys. Rev. Lett.* **1995**, 74, 1246.
- (22) Bär, M.; Kevrekidis, I. G.; Rotermund, H. H.; Ertl, G. *Phys. Rev. E* **1995**, 52(6), R5739.
- (23) Bär, M.; Bangia, A. K.; Kevrekidis, I. G.; Haas, G.; Rotermund, H. H.; Ertl, G. *J. Phys. Chem.* **1996**, 100, 19106.
- (24) Gottschalk, N.; Mertens, F.; Bär, M.; Eiswirth, M.; Imbihl, R. *Phys. Rev. Lett.* **1994**, 73, 3483.
- (25) Mertens, F.; Imbihl, R. *Nature* **1994**, 370, 124.
- (26) Vesper, G., Ph. D., Freie Universität, Berlin, 1993.
- (27) Vesper, G.; Imbihl, R. *J. Chem. Phys.* **1992**, 96, 7155.
- (28) Mertens, F.; Gottschalk, N.; Bär, M.; Eiswirth, M.; Mikhailov, A.; Imbihl, R. *Phys. Rev. E* **1995**, 51, R5193.
- (29) Mertens, F.; Imbihl, R. *Chem. Phys. Lett.* **1995**, 242, 221.
- (30) Krischer, K.; Mikhailov, A. *Phys. Rev. Lett.* **1994**, 73, 3165.
- (31) Rose, K. C.; Battogtokh, D.; Mikhailov, A.; Imbihl, R.; Engel, W.; Bradshaw, A. M. *Phys. Rev. Lett.* **1996**, 76, 3582.
- (32) Vesper, G.; Mertens, F.; Mikhailov, A. S.; Imbihl, R. *Phys. Rev. Lett.* **1993**, 71, 935.
- (33) Falcke, M.; Engel, H. *J. Chem. Phys.* **1994**, 101, 6255.
- (34) Battogtokh, D.; Mikhailov, A. *Phys. D* **1996**, 90, 84.
- (35) Battogtokh, D.; Preusser, A.; Mikhailov, A. *Phys. D* **1997**, 106, 327.
- (36) Levine, H.; Zou, X. *Phys. Rev. Lett.* **1992**, 69(1), 204.
- (37) Zhdanov, V. P.; Kasemo, B. *Surf. Sci. Rep.* **1993**, 20, 111.
- (38) Zhdanov, V. P.; Kasemo, B. *Phys. D* **1994**, 70, 383.
- (39) Zhdanov, V. P.; Kasemo, B. *Appl. Surf. Sci.* **1994**, 74, 147.
- (40) Oertzen, A. v.; Mikhailov, A.; Rotermund, H. H.; Ertl, G. *Surf. Sci.* **1996**, 350, 259.
- (41) Lauterbach, J.; Asakura, K.; Rotermund, H. H. *Surf. Sci.* **1994**, 313, 52.
- (42) Vishnevskii, A. L.; Savchenko, V. I. *React. Kinet. Catal. Lett.* **1989**, 38, 167.
- (43) Engel, W.; Kordesch, M. E.; Rotermund, H. H.; Kubala, S.; Oertzen, A. v. *Ultramicroscopy* **1991**, 36, 148.
- (44) Rotermund, H. H.; Engel, W.; Jakubith, S.; Oertzen, A. v.; Ertl, G. *Ultramicroscopy* **1991**, 36, 164.
- (45) Oertzen, A. v.; Rotermund, H. H.; Nettesheim, S. *Surf. Sci.* **1994**, 311, 322.
- (46) Rotermund, H. H.; Jakubith, S.; Oertzen, A. v.; Ertl, G. *Phys. Rev. Lett.* **1991**, 66, 3083.
- (47) Jakubith, S.; Rotermund, H. H.; Engel, W.; Oertzen, A. v.; Ertl, G. *Phys. Rev. Lett.* **1990**, 65, 3013.
- (48) Nettesheim, S.; Oertzen, A. v.; Rotermund, H. H.; Ertl, G. *J. Chem. Phys.* **1993**, 98, 9977.
- (49) Krischer, K.; Eiswirth, M.; Ertl, G. *Surf. Sci.* **1991**, 251/252, 900.
- (50) Myshlyavtsev, A. V.; Zhdanov, V. P. *Langmuir* **1993**, 9, 1290.
- (51) Persson, B. N. J. *Surf. Sci. Rep.* **1992**, 15, 1.
- (52) Imbihl, R.; Sander, M.; Ertl, G. *Surf. Sci.* **1988**, 204, L701.
- (53) Mikhailov, A. S. *Foundations of Synergetics I*, 2nd ed.; Springer-Verlag: Berlin, 1994.
- (54) Argentina, M.; Couillet, P.; Mahadevan, L. *Phys. Rev. Lett.* **1997**, 79, 2803.
- (55) Zhabotinsky, A. M.; Dolnik, M.; Epstein, I. R. *J. Chem. Phys.* **1995**, 103, 10306.
- (56) Janssen, N. M. H.; Schaak, A.; Nieuwenhuys, B. E.; Imbihl, R. *Surf. Sci.* **1996**, 364, L555.
- (57) Schedel-Niedrig, T.; Bao, X.; Muhler, M.; Schlögl, R. *Ber. Bunsen-Ges. Phys. Chem.* **1997**, 101, 994.